Electron Paramagnetic Resonance Structure Investigation of Copper Complexation in a Hemicarcerand

A. Gembus,[†] B. Corzilius,[†] R.-A. Eichel,[†] K.-P. Dinse,*[,†] S. Immel,[‡] D. Stumm,[†] M. Flauaus,[†] and H. Plenio*[,†]

Eduard-Zintl-Institute for Inorganic and Physical Chemistry, Petersenstr. 19-21, and Clemens-Schöpf-Institute for Organic Chemistry and Biochemistry, Petersenstr. 22, Darmstadt University of Technology, D-64287 Darmstadt, Germany

Received: April 6, 2006; In Final Form: May 23, 2006

The double-bridged hemicarcerand [A,B-$(CH_2OH)_2$-cavitand]-$(CH_2NHCH_2)_2$-[A,B-$(CH_2OH)_2$-cavitand] **23** (and several other related compounds) was synthesized by the condensation of the two complementary precursors A,B-$(CH_2NH_2)_2(CH_2OH)_2$-cavitand and A,B-$(CH_2Br)_2(CH_2OAc)_2$-cavitand followed by hydrolysis of the acetate groups. This hemicarcerand has nitrogen and oxygen donor atoms located on the interior of the spherical cavity and thus allows endohedral coordination of metal ions. The cavity has a volume of approximately 0.12 nm^3, a value obtained by calculating a Connolly-type contact surface and the molecular electrostatic potential. The Cu^{2+} complex of hemicarcerand **23** was studied in detail by EPR and DFT calculations at the UB3LYP/6-31G* level to verify the anticipated endohedral nature of the metal complex. It could be shown that the copper ion is coordinated to four oxygen donor atoms and no deviation from axial symmetry at the copper site could be detected. No direct coordination to nitrogen atoms of the hemicarcerand could be observed; however, complexation with DMF solvent molecules was detected by ESEEM and HYSCORE experiments. The closed structure of the hemicarcerand was also confirmed by an evaluation of proton−copper distances. Results from DFT calculations are in accord with the EPR results, and further support suggested coordination of the Cu(II) within the hemicarcerand cavity by four oxygen donor atoms.

Introduction

The outstanding properties of metalloproteins depend to a significant extent on the nature of the first coordination sphere of the active metal ion.[1] However, the influence of the enzyme pocket, which houses the substrate and that of the protein chains, shielding the active center from the environment can hardly be underestimated.[2,3] For this reason, secondary interactions of amino acids forming the pocket for the substrate and the controlled transfer of the substrate from the "aqueous phase" to the hydrophobic and poorly solvated enzyme pocket will have a significant influence on the reactivity of the substrate.[4,5]

All of the effects resulting from the environment of the first coordination sphere are difficult to model, and the approach most of bioinorganic chemistry has taken is to concentrate on the already nontrivial task of modeling the first coordination sphere of metals to produce functional and/or spectroscopic model compounds.[6] The use of bulky substituents close to the metal center is the normal approach to deal with the problems of insulating the active site from the environment and to kinetically stabilize certain metal complexes.[7] A highly innovative concept dealing with the problem of site isolation was brought forward by Reinaud et al., who used calixarene-based ligands to occupy all but a single coordination site at a metal ion.[8] Another approach is to bury a metal complex within a polymeric or dendritic structure,[9,10] while the Matt group places organometallic groups within the cavity of calixarenes.[11]

We want to apply the concept of site isolation and encapsulation by building large molecules which have interior cavities large enough to accommodate molecules. Furthermore, the host should possess metal coordinating groups on the inside of the cavity, to allow the endohedral complexation of metal ions. Cram's cavitands, hemicarcerands, and carcerands appear to be best suited for this type of chemistry,[12] even though other cavity-forming molecules such as cyclodextrins, calixarenes, capped porphyrins, or cucubituril might be also used.[13−17] Metal complexes of cavitands are known.[18−21] In all of these examples, the metals are, however, located outside the cavity or are part of the exterior wall.[22]

In contrast, invoking the concept of linking two cavitands in a semiflexible way should give rise to metal ion localization in the interior of the hemicarcerand. Lacking the possibility to explore the structure directly by X-ray methods, the more indirect magnetic resonance methodology was invoked. A detailed electron paramagnetic resonance (EPR) study of Cu(II) [A,B-$(CH_2OH)_2$-Cav]-$(CH_2NHCH_2)_2$-[A,B-$(CH_2OH)_2$-Cav] hemicarcerand **23** (see Scheme 2) was therefore undertaken in order to elucidate the binding mode of the metal ion and its location. Continuous-wave (CW) EPR can be used to reveal the $\boldsymbol{g}$-matrix and the hyperfine coupling (hfc) tensor of the copper ion. Comparing these EPR data to previous results from similar compounds should allow for a first guess of the complex geometry and its first coordination sphere. Unambiguous identification and quantification of ligands, however, requires detection of small hyperfine interactions (hfi) with local and remote nuclear spins. Pulse EPR techniques such as ESEEM (electron spin−echo envelope modulation) and HYSCORE (hyperfine sublevel correlation) experiments are necessary to

* Corresponding authors. E-mail addresses: dinse@chemie.tu-darmstadt.de; plenio@tu-darmstadt.de.
[†] Eduard-Zintl-Institute for Inorganic and Physical Chemistry.
[‡] Clemens-Schöpf-Institute for Organic Chemistry and Biochemistry.

10.1021/jp062158x CCC: $33.50
Published on Web 07/13/2006

SCHEME 1: Synthesis of the Monobridged Hemicarcerands

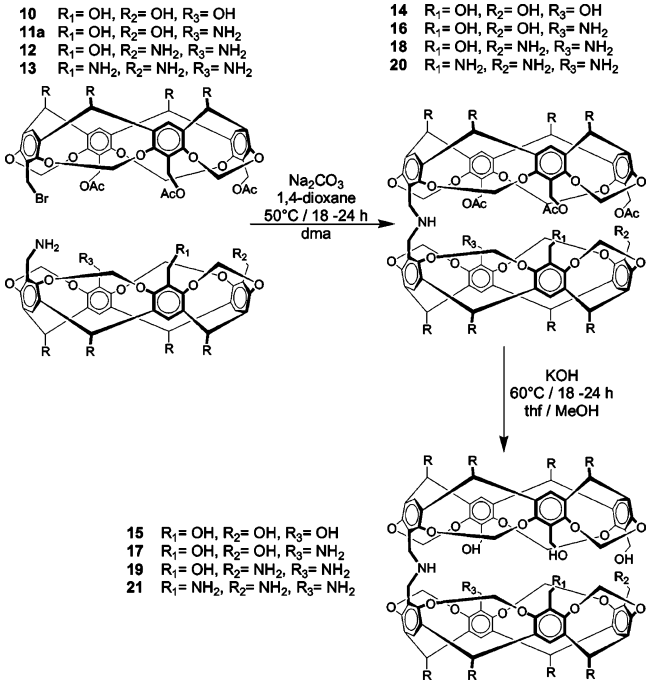

SCHEME 2: Synthesis of the Double-Bridged Hemicarcerands

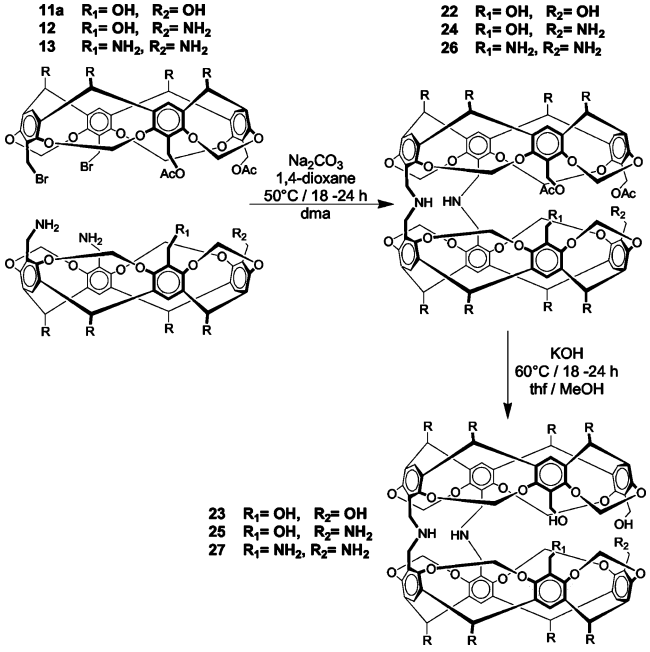

deduce this information from a disordered sample. For a discrimination between "open" and "closed" structures, we planned to measure distances between the metal position and specific proton positions of the hemicarcerand. It was also of interest to probe whether the rather large internal volume of the hemicarcerand is occupied by solvent molecules. Such a situation should give rise to axial coordination with the metal center.

Experimental Section

Synthesis of the Cavitands, Hemicarcerands, and Their Metal Complexes. We have recently described the functionalization of the tetrapropyl-footed $(CH_2Br)_4$ cavitand by reaction with NaOAc to produce the various organic acetates in excellent yields.[23] To increase the solubility of the respective hemicarcerands, we now applied the same method to the tetrapentyl-footed $(CH_2Br)_4$ cavitand to result in the formation of the various $(CH_2Br)_n(CH_2OAc)_{4-n}$ cavitands ($n = 0-3$) in a larger than 95% overall yield. The various $(CH_2Br)_n(CH_2OAc)_{4-n}$ cavitands were converted into the respective $(CH_2NH_2)_n(CH_2OH)_{4-n}$ cavitands via Gabriel synthesis ($-CH_2Br \rightarrow -CH_2NH_2$) and hydrolysis of the ester groups ($-CH_2OAc \rightarrow -CH_2OH$).

To synthesize hemicarcerands,[24] which are composed of two hemispherical molecules, two cavitands with complementary functional groups are needed, such as the $(CH_2Br)_n(CH_2OAc)_{4-n}$ cavitands and $(CH_2NH_2)_n(CH_2OH)_{4-n}$ cavitands described here. The condensation of $-CH_2Br$ and $-CH_2NH_2$ groups from two cavitands results in the formation of the desired monobridged hemicarcerands **14**−**21** and double-bridged hemicarcerands **22**−**27**, as shown in Schemes 1 and 2.

We have synthesized mono- and double-bridged species in excellent yields, typically >90%, but the use of 1,4-dioxane as a template is crucial for the assembly of the two cavitand shells. The importance of using suitable templating molecules has already been demonstrated by the Sherman group, in the synthesis of related carcerands.[25] In the reactions leading to the A,B-bridged hemicarcerand, in principle, two different isomeric products are possible. As evidenced by thin-layer chromatography (TLC) and NMR spectroscopy, we obtain without exception only a single isomer from our reaction, which we assign to be the closed form, which is favored by hydrogen bonding and appears to be the typical isomer in such compounds. We are only aware of a single report from Cram et al.[26] in which an open hemicarcerand is formed.[27] Another argument in favor of the closed isomer is the efficient formation of **23** which only occurs in the presence of a templating molecule identical to the one used by Sherman et al. for the formation of hemicarcerands.[25] More discussion on the structure assignment can be found in the EPR section. Metal complexes of the hemicarcerand **23** were synthesized by mixing THF solutions of hemicarcerand and the respective metal salts $Ni(SO_3CF_3)_2$ or $Ni(ClO_4)_2$ and $Cu(SO_3CF_3)_2$ and heating to 55 °C for 60 h. Precipitation of the complexes with diethyl ether gave the respective metal complexes in quantitative yields. The stoichiometry composition of the complex was established by elemental analysis. All attempts to obtain single crystals of such complexes for X-ray crystal structure determinations were unsuccessful. UV−vis spectra of the metal complexes [10^{-3} M] revealed weak d−d transitions for the complexes of Cu^{2+} ($\lambda_{max} = 675$ nm). We also studied the magnetism of **23**·$Ni(SO_3CF_3)_2$. The free induction decay (FID) and the ^1H NMR spectrum of this complex provide unequivocal evidence of the diamagnetic nature of this complex, which points to a square-planar coordination sphere of Ni^{2+}.

EPR Spectroscopy. *CW EPR.* X-band continuous-wave (CW) EPR experiments were performed on a Bruker ESP 300E spectrometer at a microwave (mw) frequency of 9.3 GHz, equipped with a rectangular TE_{102} resonator (Bruker 4102 ST). For a variation of the temperature below 140 K, a helium-flux cryostat (Oxford, ESR 900) was used. At higher temperatures, a nitrogen-cooled quartz finger Dewar was utilized instead.

Pulse EPR. The X-band pulse EPR measurements were performed at 9.7 GHz and a temperature of 10 K on a Bruker ElexSys 680 spectrometer, using a cylindrical TE_{011} dielectric-ring resonator (Bruker, EN 4118 X-MD-4). The temperature was varied with a helium-flux cryostat (Oxford, CF 935 STD) and controlled with a PID temperature control unit (Oxford,

ITC 503). For both spectrometers, the magnetic field was measured with an NMR gaussmeter (Bruker, ER 035M).

Echo-Detected EPR. Field-swept electron spin−echo detected EPR spectra were recorded as a function of the external field by employing a two-pulse echo sequence ($^{\pi}/_{2} - \tau - \pi - \tau -$ echo) and integrating over the whole width of the echo. The lengths of the mw pulses were $t_{\pi/2} = 16$ ns and $t_{\pi} = 32$ ns.

ESEEM. Three-pulse ESEEM spectra were obtained by employing a stimulated-echo sequence ($^{\pi}/_{2} - \tau - {}^{\pi}/_{2} - T - {}^{\pi}/_{2} - \tau -$ echo) and sampling the echo amplitude as a function of the interpulse time T. To enhance the modulation depth, the signal was integrated using a small time interval centered at the maximum of the echo. The time-domain data was then corrected by a third-order polynomial baseline. The final frequency-domain ESEEM spectra were obtained after an apodization with a Hamming window function and zero filling to 2048 data points with subsequent 1D Fourier transformation.

HYSCORE. HYSCORE spectra were recorded using the four-pulse sequence ($^{\pi}/_{2} - \tau - {}^{\pi}/_{2} - t_1 - \pi - t_2 - {}^{\pi}/_{2} - \tau -$ echo) and a four-step phase cycle in order to remove artifacts from unwanted echoes.[28] The following parameters were employed: $t_{\pi/2} = 16$ ns, $t_{\pi} = 24$ ns, $\tau = 200$ ns, and starting times $t_1^s = t_2^s = 100$ ns. The echo was recorded as a function of t_1 and t_2, which were incremented in steps of 8 ns. For the "matched" HYSCORE experiment, the second, third, and fourth pulses were chosen as 44, 16, and 44 ns, respectively. In both dimensions, 512 data points were collected. The recorded time-domain data was processed as follows: the background echo decay in both t_1 and t_2 dimensions was removed by least-squares fitting to a second-order polynomial followed by subtraction. Both dimensions of the data were then convoluted with a Hamming window function for apodization, zero-filled to 1024 data points and 2D Fourier transformed, giving the frequency-domain HYSCORE spectrum. The spectra presented in this paper are contour plots with linear scaling after magnitude calculation. These appear in two quadrants, referred to as the positive (+, +) and negative (+, −) quadrants.

DFT Calculations. Molecular models of the Ni^{2+} and Cu^{2+} hemicarcerand complexes (all *n*-pentyl side chains replaced by hydrogen atoms) were obtained from DFT calculations. Full energy optimization (B3LYP and UB3LYP, respectively) was performed using a 6-31G* basis set for the ligand, augmented by additional polarization and diffuse functions (6-311+G** basis) for the polar $M^{2+}[(^{-}OCH_2)_n(HOCH_2)_{4-n}]$ core regions of the complexes, as well as for the two $-CH_2-NH_2^{+}-CH_2-$ linkers. The central transition metal ions were represented by a LACV3P+**-type effective core potential (ECP)[29] including metal diffuse d-functions; optimizations were carried out using the *Jaguar*[30] program. Structural analysis and generation of all molecular graphics was performed using the *MolArch*$^{+}$ program.[31] The complex analysis yielded the following structural parameters.

Ni^{2+} complex (charge = +2, multiplicity = 1): $[C_{72}H_{62}O_{20}N_2\text{-}Ni]^{2+}$, Ni^{2+}[A-(CH_2O^{-})-B-(CH_2OH)-Cav]-$(CH_2NH_2^{+}CH_2)_2$-[A-(CH_2OH)-B-(CH_2O^{-})-Cav], symmetry C_2, $E = -4563.823\,950$ h, $d_{Ni-O} = 1.907$ and $d_{Ni-OH} = 2.063$ Å, $d_{O-O} = 2.386$ and 3.123 Å, Ni^{2+} out-of-plane deviation 0.292 Å.

Cu^{2+} complex (charge = 0, multiplicity = 2): $[C_{72}H_{60}O_{20}N_2\text{-}Cu]^{0}$, Cu^{2+}[A,B-$(CH_2O^{-})_2$-Cav]-$(CH_2NH_2^{+}CH_2)_2$-[A,B-$(CH_2O^{-})_2$-Cav], symmetry C_{2v}, $E = -4589.794\,393$ h, $d_{Cu-O} = 1.995$ Å, $d_{O-O} = 2.779$ and 2.802 Å, Cu^{2+} out-of-plane deviation 0.294 Å. Further details about the computational procedure are listed in the Supporting Information.

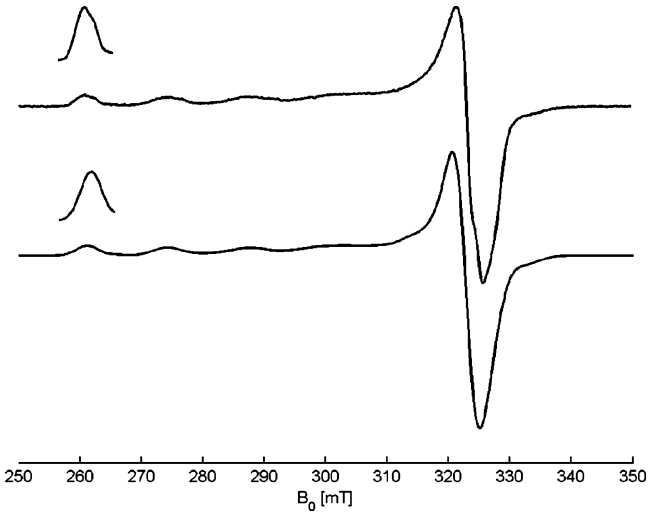

Figure 1. Experimental EPR spectrum of the Cu(II) hemicarcerand **23** taken at 9.375 GHz and a temperature of 10 K (upper trace) and its numerical simulation (lower trace).

Results and Discussion

Surface Properties and Cavity Dimensions. To evaluate the cavity dimensions and the properties of the ligand, its Connolly-type contact surface[32] has been generated for the PM3 optimized geometry of **23**.

As shown in the Supporting Information, the cavity itself exhibits an elongated ellipsoidal shape with a volume of approximately 0.12 nm^3. Both ends of the cavity display a negative polarized surface due to the circular alignment of phenolic and acetalic oxygen atoms. This polar environment renders the central cavity the most hydrophilic part of the ligand as compared to the rather hydrophobic surface regions made up of the *n*-pentyl side chains protruding from both ends of the molecule. On the basis of the cavity volume, it seems possible that an additional solvent molecule is coordinated endohedrally to the metal ion. The molecular volume of tetrahydrofuran (THF) is approximately 0.09 nm^3, and thus for steric reasons, the cavity may be suitable to accommodate THF. The ligand may also bear some inherent flexibility by bending along its central axis, to allow potential guest molecules to enter the central cavity, which otherwise seems to be fully closed in the geometry. By bending, which is certainly energetically favorable compared to the relative rotation of both calixarene subunits against each other due to their linkage via two nitrogen atoms, the size of the cavity may also increase and adapt its shape to additional ligands in the complex.

Spin Hamiltonian. An adequate spin Hamiltonian for a $3d^9$ ion with an $S = {}^{1}/_{2}$ electron spin interacting with N nuclei of arbitrary nuclear spin I is given by

$$\mathcal{H} = \beta_e \mathbf{B}_0 \cdot \mathbf{g} \cdot \mathbf{S} - \sum_{i=1}^{N} g_{n,i}\beta_n \mathbf{B}_0 \cdot \mathbf{I}_i + \sum_{i=1}^{N} \mathbf{S} \cdot \mathbf{A}_i \cdot \mathbf{I}_i + \sum_{I \geq 1} \mathbf{I}_i \mathbf{Q}_i \mathbf{I}_i \quad (1)$$

The nuclear g factors and the Bohr and nuclear magnetons are denoted by $g_{n,i}$, β_e, and β_n, respectively. The first two terms describe electronic and nuclear Zeeman interactions; the last terms give the hyperfine interaction to adjacent magnetic nuclei and the nuclear quadrupole interaction for nuclei with $I \geq 1$. $\mathbf{B}_0$ describes the external field. $\mathbf{B}_0$, the hyperfine tensors $\mathbf{A}_i$, and the quadrupole tensors $\mathbf{Q}_i$ are defined in the principal axes system of the **g**-matrix. The index i refers to particular nuclei.

Although hfi with ^{14}N cannot be resolved by EPR, both hyperfine and nuclear quadrupole interactions have to be

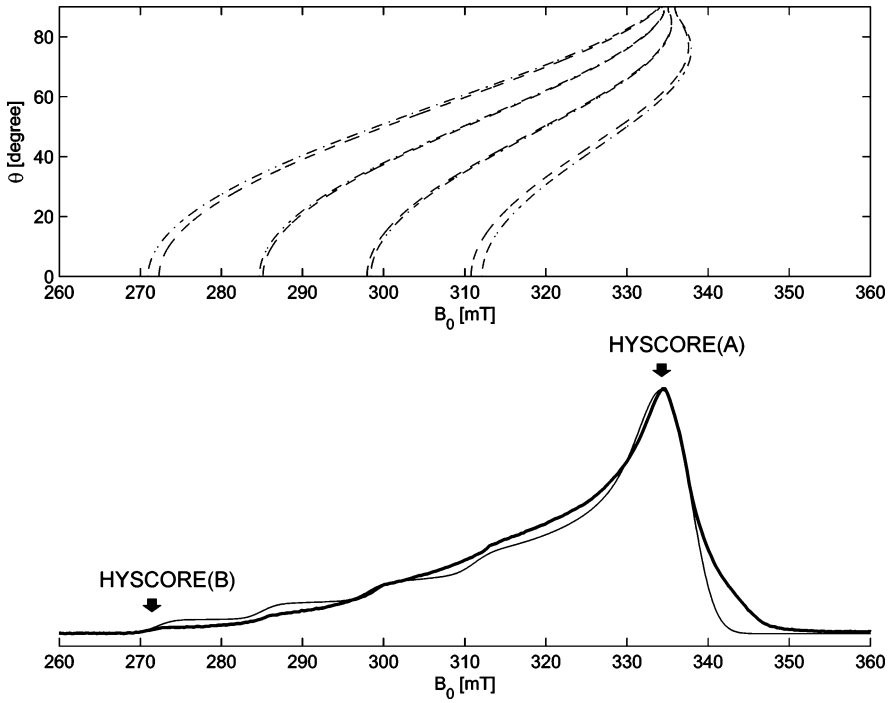

Figure 2. In the lower part, the primary echo-induced EPR spectrum of the Cu(II) hemicarcerand **23** at 9.73 GHz and 10 K in THF (thick line), as well as the numerical simulation (thin line) for one species, is presented. In the upper part, the orientation dependence of the numerically simulated species is shown for the angle θ with respect to $\mathbf{B}_0$. The isotopes of ^{63}Cu and ^{65}Cu are displayed by dashed and dashed−dotted lines.

considered for evaluation of ESEEM and HYSCORE spectra. HYSCORE correlation peaks (ν_α, ν_β) and (ν_β, ν_α) are split into multiplets depending upon the size of the quadrupole coupling constant $\kappa = e^2qQ/4h$ and the asymmetry parameter $\eta = |(Q_{xx} - Q_{yy})/Q_{zz}|$, which is defined by the diagonal elements of the traceless quadrupole tensor using standard notation.

At X-band frequencies, often the so-called "cancellation condition" is met, for which one has $2\nu_I \approx |A|$. As a result, the effective field experienced by one of the two m_S manifolds vanishes because nuclear Zeeman and hyperfine interaction cancel each other. One therefore finds narrow zero-field quadrupole transitions even in a disordered sample. The nuclear transition frequencies of the m_S manifold, in which the hyperfine and the Zeeman fields add rather than cancel each other, are denoted as single-quantum $\nu^{sq}_{1,2}$ ($\Delta m_I = \pm 1$) and double-quantum ν^{dq} ($\Delta m_I = \pm 2$) transitions, the latter found at

$$\nu^{dq} \approx 2\left[\left(\left|\nu_I\right| + \left|\frac{a_{iso}}{2}\right|\right)^2 + \kappa^2(3+\eta^2)\right]^{1/2} \qquad (2)$$

The expression for the double quantum transition frequency ν^{dq}, however, is only approximately valid even under the assumption that the anisotropic part of the hyperfine interaction can be neglected. Equation 2 can nevertheless be used to obtain an estimate of the dipolar hfi, even though only "nuclear quadrupole frequencies" are observed.

In the electronic spin level, in which hyperfine and nuclear Zeeman interactions nearly cancel, nuclear spin transitions are predicted to occur at frequencies close to

$$\nu_0 = \frac{e^2qQ}{2h}\eta = 2\kappa\eta \qquad (3)$$

$$\nu_\pm = \frac{3e^2qQ}{4h}\left(1 \pm \frac{\eta}{3}\right) = \kappa(3 \pm \eta) \qquad (4)$$

EPR−Results. An EPR spectrum of the hemicarcerand complex in d_8-THF is presented in Figure 1. Line broadening originating from dipolar interaction can be excluded because of the small concentration (10^{-4} M) used.

The line width is determined either by unresolved hyperfine interactions or by a variation of **g**-matrix values or copper hfi tensor elements. As expected for a $3d^9$ ion with $I = {}^3/_2$ nuclear spin, a well-resolved quartet in the region of $g_{||}$ is observed. However, at $g_\perp$, copper hfc is not resolved because of overlapping resonances from different orientations. A striking observation in the hemicarcerand spectrum is the shape of the low-field absorption edge (inset in Figure 1). This structure shows an intensity ratio contrary to that expected for an isotope multiplet. Thus, we had to assume that two different Cu(II) species are present, a hypothesis which was confirmed by recording EPR spectra as a function of both temperature and mw power. Partial separation of both components was possible because of slight differences in inhomogeneous line widths and saturation properties.

A Hahn echo-induced EPR spectrum is depicted in Figure 2, showing also the observer position for the HYSCORE experiments, as well as a simulation of the orientation dependence of the resonance lines.

Refined spin Hamiltonian parameters were obtained from the spectrum of the Cu(II)complex of **23** taken at 10 K in d_8-THF by numerical spectrum simulation. According to the fact that the complex apparently has axial symmetry, values for $g_\perp = 2.074$ and $g_{||} = 2.385$ are obtained (Figure 2). The values for the hyperfine coupling constants of $A_\perp^{63Cu}$ and $A_{||}^{63Cu}$ are 16 and 428 MHz, respectively. As a consequence, 17.1 and 458 MHz for $A_\perp^{65Cu}$ and $A_{||}^{65Cu}$ are determined for the other isotope. The best reproduction of the experimental spectra could be achieved for the main axes system of the **g** and $\mathbf{A}^{Cu}$ matrixes being collinear.

Simulation assuming axial symmetry also for the second Cu(II) complex yields $g_\perp = 2.045$ and $g_{||} = 2.32$. Copper hfcc are $A_\perp^{63Cu} = 24$ MHz, $A_{||}^{63Cu} = 520$ MHz, $A_\perp^{65Cu} = 25.7$ MHz, and $A_{||}^{65Cu} = 556.4$ MHz. For the main component, a line width

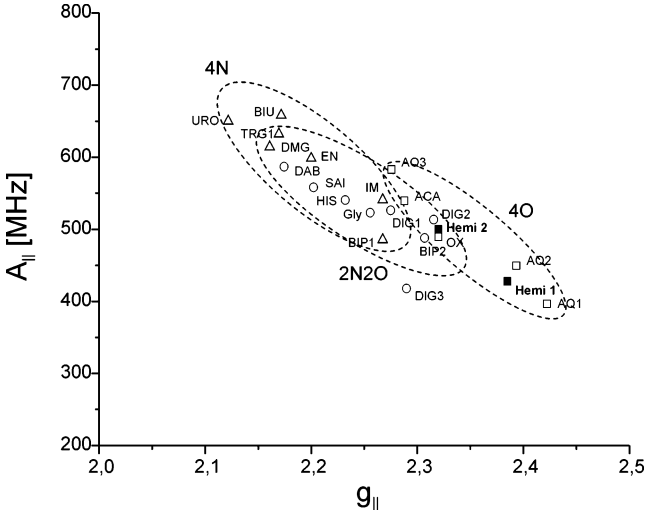

Figure 3. Cu complexes with various ligand compounds are depicted as a function of $A_{||}$ with respect to $g_{||}$.[33] Open symbols characterize complexes, in which the Cu center is complexed either by four nitrogen atoms (up-triangles), two nitrogen and two oxygen atoms (circles), or four oxygen atoms (squares). The values for both Cu(II) hemicarcerands are represented by filled squares. Hemi1 indicates the main and Hemi2 the second component, present with relative intensities 95:5.

(fwhm) of 50 MHz is found, whereas the second Cu(II) complex exhibits a broader width of 60 MHz. After summation of both spectra with relative weight 95:5, a good fit of the spectrum observed at 10 K is obtained.

With the accurately determined values for $g_{||}$ and $A_{||}^{Cu}$ taken into account, the so-called "Peisach−Blumberg plot",[33] illustrated in Figure 3 can be used to deduce information about the type and number of ligands. Obviously, the values for Hemi1 lie in a region characteristic for coordination to four oxygens. We therefore conclude that the major Cu(II) center of the hemicarcerand is complexed by four oxygen atoms, with the number of axial ligands not being defined. The suggested exclusive ligation by oxygen is confirmed by ENDOR and HYSCORE experiments (see below).

For Hemi2, the situation is less clear. Complexation of the copper ion by two oxygen and two nitrogen atoms is unlikely for steric reasons because of the large distances to oxygen and nitrogen atoms. Assuming that complexation to four oxygen atoms prevails, we could conclude that the decrease of the **g**-matrix components points to a higher spin density at the metal center of the second complex. The increase of the copper hfi tensor components indicates a stronger interaction to remaining coordination partners.

In the case of Hemi1, we could prove that complexation with a single solvent molecule dimethylformamide (DMF) occurs (see below). We, thus, tentatively attribute changes in spin Hamiltonian parameters of Hemi2 to a loss of solvent coordination. A similar behavior has been found for an α-hydroxycarboxylic acid-chelated Cr(V) complex, for which *g*- and *A*-values depend on mono- or bis-chelatisation.[34] For the bis-chelated Cr(V) complex in methanol, no solvent molecules take part in stabilization, whereas in the case of complexation in methanol in the presence of bases, one α-hydroxycarboxylic acid and three coordinating methoxy groups were observed. The resulting *g*-values differ in the third decimal place, and values for the hyperfine splitting constants $A_{||}$ differ by about 7%. Roughly the same changes are observed for both Cu(II) hemicarcerand components: *g*-values also vary by 10^{-3}, and the values for $A_{||}$ differ by 5%.

Nitrogen ENDOR and HYSCORE Experiments. To confirm our conclusion about complexation by four oxygen atoms, ENDOR experiments were performed, probing for strongly coupled nitrogen spins. No such signals could be detected. In contrast, signals were found which could tentatively be attributed to nitrogen spins with rather weak hfi. These signals could either arise from solvent molecules or from distant nitrogen atoms of

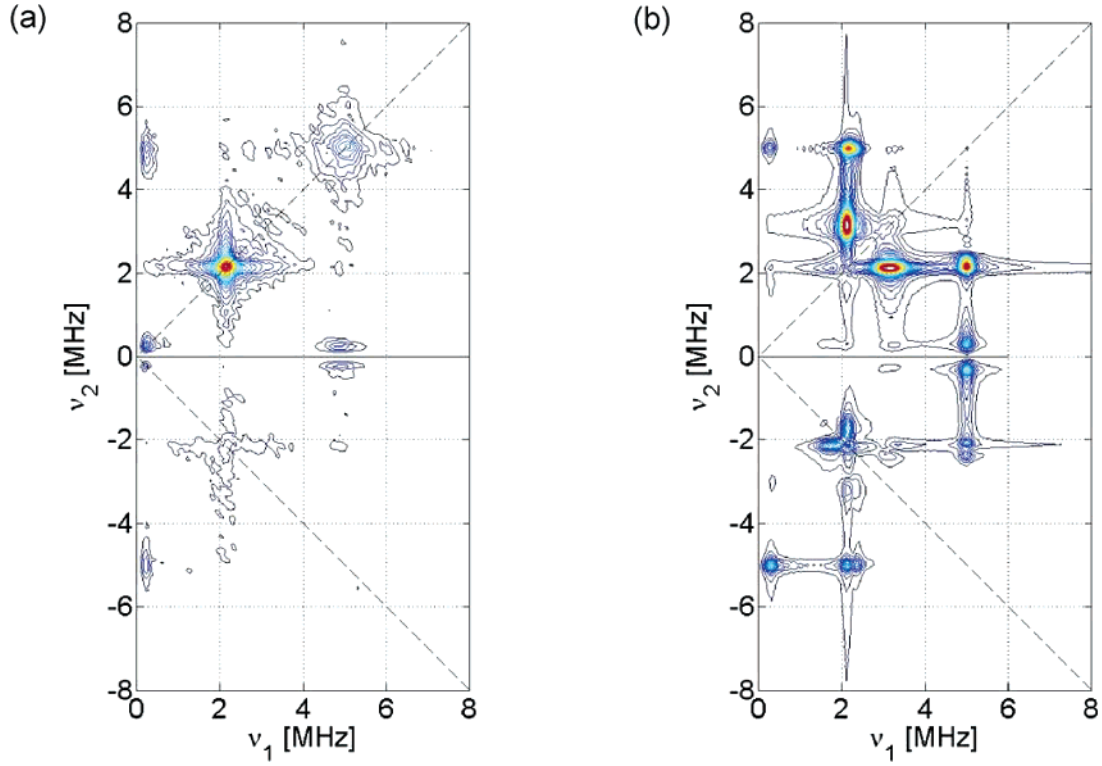

Figure 4. (a) Experimental ^{14}N-HYSCORE spectrum of the Cu(II) hemicarcerand **23** in DMF, at 9.73 GHz and 10 K for the observer position A in Figure 2. (b) Numerical simulation.

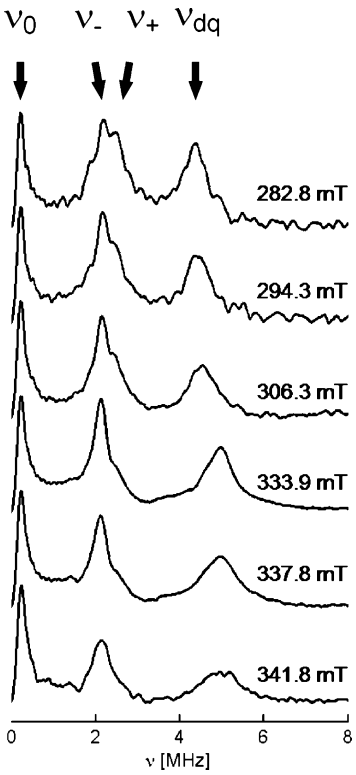

Figure 5. Orientation-dependent ESEEM experiments for the labeled ^{63}Cu(II) ^{15}N hemicarcerand **23** in ^{14}N-DMF at 9.73 GHz and 10 K.

TABLE 1: Proton hf Tensor Elements for Three Identified Positions

	set I	set II	set III
$A_{\perp}(^1\text{H})$ [MHz]	1.10	4.00	−9.65
$A_{\|\|}(^1\text{H})$ [MHz]	3.85	8.80	10.45
Eulerian angle β [°]	0.00	0.00	5.00
$a_{iso}(^1\text{H})$ [MHz]	2.02	5.60	−2.95
$T(^1\text{H})$ [MHz]	0.92	1.60	6.70

23. To discriminate between these possibilities, the ^{15}N-labeled hemicarcerand was studied in DMF. Under this condition, any observed ^{14}N hfcc can only arise from interaction with solvent molecules. A convenient method to detect such weak interactions is given by performing a HYSCORE experiment. The resulting ^{14}N-HYSCORE spectrum is shown in Figure 4a.

The observed pattern is characteristic for ^{14}N in a "cancellation regime", frequently seen for remote nitrogen atoms at the X-band.[35] Hence, the observed correlation peaks correspond to correlation peaks of ^{14}N NQR transitions with the double-quantum frequency defined in eq 2; $(\nu_0, \nu^{dq}) = (0.22, 4.98)$ MHz, $(\nu_-, \nu^{dq}) = (2.12, 4.98)$ MHz, and $(\nu_+, \nu^{dq}) = (2.34, 4.98)$ MHz, corresponding to $\eta = 0.148$, $\kappa = 0.743$ MHz. Correlations to the single-quantum transitions $\nu^{sq}_{1,2}$ were not observed, probably because of the orientation dependence resulting predominantly from quadrupole interaction. A simulated HYSCORE spectrum is depicted in Figure 4b. The best agreement with the experimental HYSCORE pattern is obtained when using an isotropic nitrogen hfcc and an Eulerian angle β of 80 ° between **g**-matrix and quadrupolar tensor principal axes.

Once peak assignment is obtained with HYSCORE, the orientation dependence of the nuclear quadrupole peaks can be probed by three-pulse ESEEM (Figure 5) in much less time.

It was thus possible to monitor the position of the double-quantum frequency ν^{dq} as function of B_0 for the full field range. The observed field dependence indicates that observed frequency shifts are caused predominantly by the nuclear Zeeman contribution. Thus, the nitrogen hfi tensor can be assumed to be almost isotropic, consistent with the finding from the HYSCORE simulation.

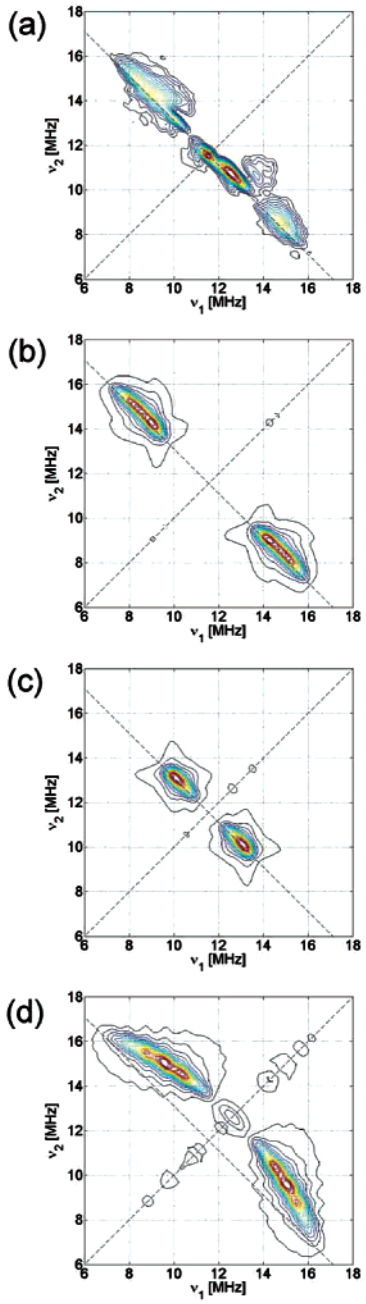

Figure 6. (a) "Matched" ^{1}H-HYSCORE spectrum of the Cu(II) hemicarcerand **23** in d^8-THF at 9.72 GHz and 10 K for the observer position B in Figure 2. (b−d) Numerical simulations for the sets of protons listed in Table 1.

TABLE 2: EPR vs DFT Distances

	^{1}H···Cu distances [nm]	
set	EPR	DFT
I	0.44	0.42
II	0.36	0.33
		0.37
III	0.23	0.27

Proton HYSCORE Experiments. For further confirmation of the proposed closed structure of **23**, an estimate for the distance of hydrogen positions to the metal center was obtained by determining the traceless part of the proton hfi by HY-

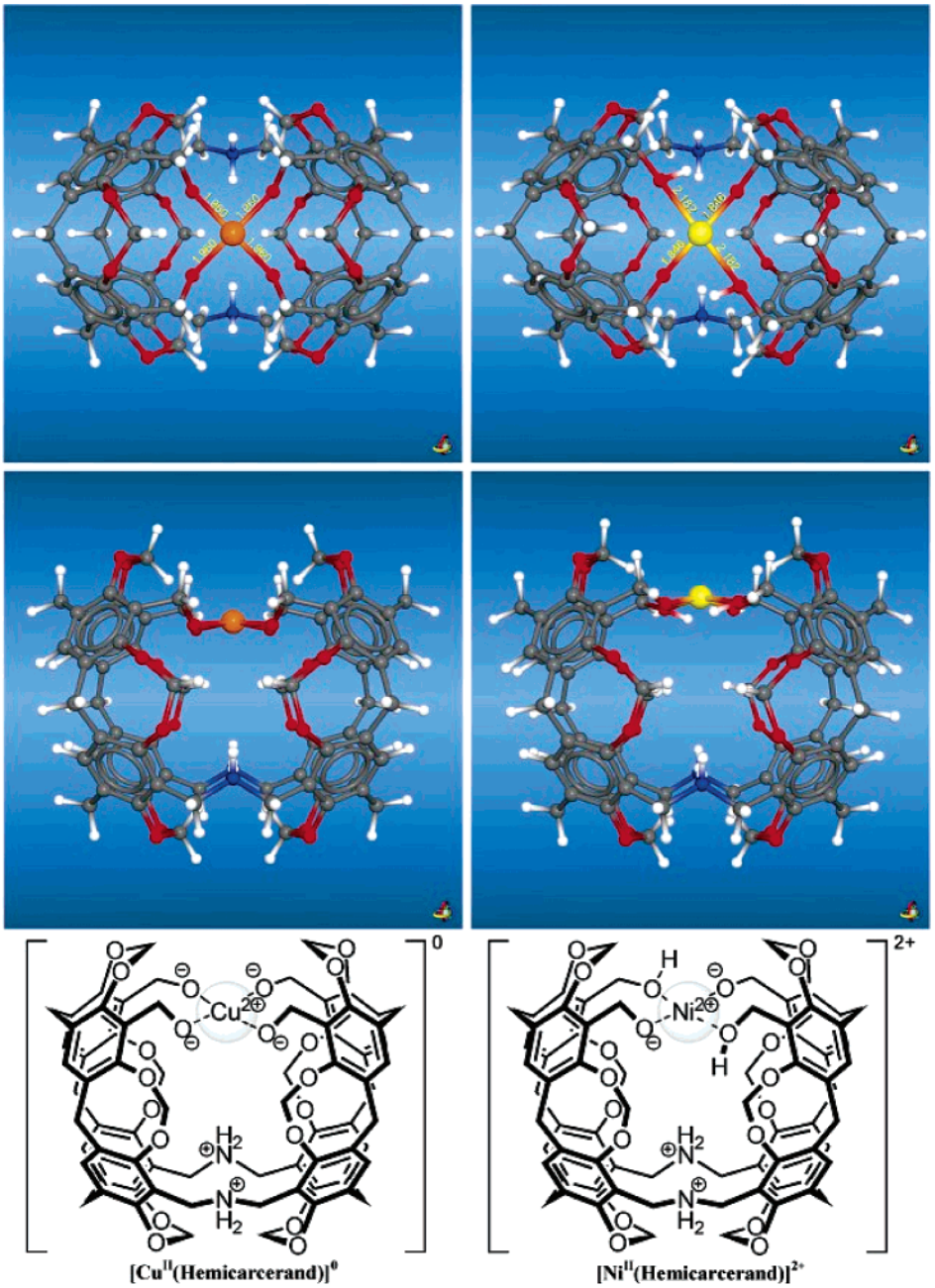

Figure 7. Proposed structures (top and side views) of metal complexes of the hemicarcerand **23** (*n*-pentyl side chains replaced by hydrogen): on the left, the neutral Cu^{II} complex ($[Cu^{2+}(^{-}OR)_4]^{2-}$, both N-linkages protonated, symmetry C_{2v}, UB3LYP geometry) is depicted; on the right, the corresponding Ni^{II}-complex structure is given ($[Ni^{2+}(^{-}OR)_2(HOR)_2]^0$, both N-linkages protonated, symmetry C_2, B3LYP optimized structure); DFT calculations employing a 6-31G* basis set for the ligand, in conjunction with an extended 6-311+G** basis for the polar $M[(^{-}OCH_2)_n(HOCH_2)_{4-n}]$ complex core region and the $-CH_2-NH_2^{+}-CH_2-$ linkers, combined with a LACV3P+** effective core potential (ECP) for the transition metal center.

SCORE. In anticipation of axial symmetry of this second-rank tensor, the analysis of two-dimensional HYSCORE spectra allows one to deduce its principal value. The copper complex of **23** dissolved in d_8-THF was investigated, to avoid interference from hfi with solvent molecules. Contributions originating from three different centers can be distinguished in the spectra as shown in Figure 6a. Such deconvolution is only possible by invoking a 2D approach, because in ENDOR, all spectral components would overlap in the vicinity of the free proton frequency. In Figure 6b−d, spectra simulated separately for each component are shown, to facilitate comparison with the experimental data. Hfi tensor sets used for simulation are compiled in Table 1. By invoking a simple point dipole model, these values can be converted into distances.

Close coincidence (Table 2) was found with values predicted for proton positions in the DFT-optimized closed structure as indicated in Figures 7 and 8. (The small difference predicted for sets IIa and IIb cannot be resolved by HYSCORE.) This assignment is supported by DFT-derived spin densities, predicting a negative spin density for the group of protons at closest distance. DFT-derived Mulliken spin densities of the full energy optimized Cu^{2+} hemicarcerand indicate negligible isotropic contributions at the observed hydrogen atoms; all hydrogen spin densities are less than 0.5% with respect to the copper ion. Thus, estimation of distances between the paramagnetic center and the hydrogen atoms by point−dipole approximation seems appropriate.

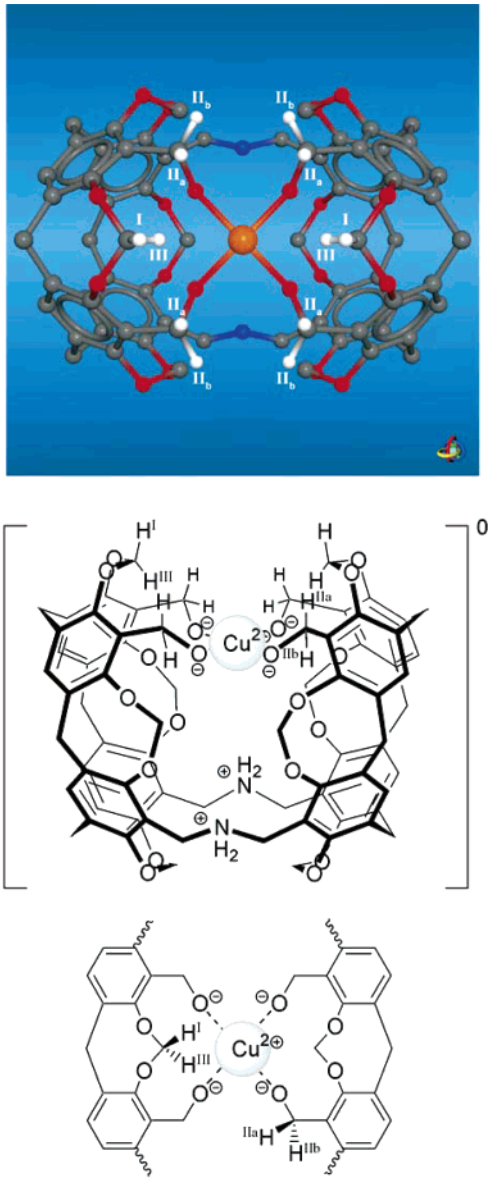

Figure 8. Environment of chemically nonequivalent protons around the central metal ion of the hemicarcerand Cu^{II} complex. By EPR measurements, three distinct groups of protons I, II, and III have been identified. Derived proton−copper distances (for proton labels, see Table 2) are well in agreement with the expectation values taken from the DFT structure (Figure 7). Protons IIa and IIb were not resolved separately. Chemical formulas provide side- and top-view projections of the complex with one set of protons labeled and displaying the axial symmetry around the metal core.

DFT Modeling of the Metal Complexes of Hemicarcerand 23. Ab initio (DFT and UDFT) calculations on model compounds for the hemicarcerand **23** metal complexes (R = *n*-pentyl side chains replaced by hydrogen only) confirmed the structural model, by which copper is complexed by four oxygen atoms. Electrostatic interactions of the four ligands' benzylic hydroxyl groups in endohedral orientation with the twofold positively charged metal ions are sufficiently attractive to form stable complexes, particularly if all four or only two of the hydroxyl groups are deprotonated and the protons are shifted toward the basic nitrogen atoms. Slight elliptical distortions of the cavitand spheres enable the O···O distances to decrease to about 0.28 nm (within each cavitand sphere as well as across the ligands gap), thus forming nearly square planar complexes with both Cu^{2+} and Ni^{2+} ions (unlike the nitrogen atoms, the hydroxyl groups are not involved in the rather rigid linkages of the two cavitand units, and therefore, ring distortions are more likely to occur in their positions). Figure 7 displays fully optimized geometries of these complexes based on these calculations. Thereby, the Cu complex was generated in its neutral form (four alcoholates bound to Cu^{2+}, both nitrogen positions protonated), whereas the Ni^{2+} complex is of the $Ni^{2+}(^{-}OR)_2(HOR)_2$ type (nitrogens protonated, total charge = +2). All calculations displayed a clear tendency to converge toward structures of higher symmetry, and therefore, these complexes belong to the C_{2v} (Cu^{2+}) and C_2 (Ni^{2+}) point groups. In the latter species, rapid exchange of the hydroxyl protons in the ROH···$^{-}$OR fragments within the metal core may also lead to time-averaged geometries of C_{2v} symmetry. The geometry of the Cu species given in Figure 7 is consistent with the EPR data presented in this work, particularly in view of the experimental finding of axial symmetry in the coordination sphere with respect to the central metal cation. In these square planar complexes, the metal ions are only slightly displaced out of the mean plane formed by the surrounding oxygens (Cu^{2+}, 0.0294 nm; Ni^{2+}, 0.0292 nm). From the viewpoint of a coordination chemist, the preference of O- vs N-coordination is surprising but can be rationalized on the basis of two arguments: The above-mentioned geometry restrictions concerning the two bridging nitrogen atoms disfavor a chelating nitrogen coordination, and furthermore, the two nitrogen atoms in the cavitand's linkers may act as a base toward the alcohol ligands in the Lewis acid environment of the metal cations.

Conclusion

Linking two hemispherical cavitand molecules via two $-CH_2-NHCH_2-$ bridging units results in the formation of a mussel-type hemicarcerand with an internal volume of around 0.12 nm^3 as determined by a Connolly-type contact surface method. The geometric setup of the donor atoms thus in principle allows the coordination of metal ions within the interior volume of the cavity. In the absence of single crystals, computational and EPR methods were utilized to provide information on the nature of the metal complexes. EPR measurements of Cu(II) hemicarcerand **23** revealed the existence of two different Cu(II) complexes in a ratio of 95:5. There is clear evidence that in both cases Cu(II) is complexed to four oxygen atoms within the cavity of the hemicarcerand because of the lack of hfi with directly bound nitrogen. This conclusion is in agreement with qualitative arguments on the basis of a Peisach−Blumberg plot, when exploiting the experimental $g_{\|}$ and $A_{\|}^{Cu}$ values. It is suggested that both components differ in the number and/or position of axially ligating solvent molecules. Evaluation of dipolar hfi with local protons resulted in three sets of distances to the metal center, which nicely agreed with distances found in a DFT-optimized "closed" structure of the hemicarcerand. Ligation to solvent molecules was detected via nitrogen hfi (in case of DMF) or deuterium hfi (in case of d_8-THF). However, it could not unambiguously be decided whether the ligated solvent molecule is located within the cavity of the hemicarcerand.

Acknowledgment. We are grateful for helpful discussions with E. Ramić, and to M. Reggelin for providing additional computing time. This research has been supported by the DFG priority program 1051 "High-field EPR in Biology, Chemistry and Physics" (Di 182/21-2). Support of this work by the DFG (Pl 178/6) is acknowledged.

Supporting Information Available: Synthesis information and additional experimental data. This material is available free of charge via the Internet at http://pubs.acs.org.

References and Notes

(1) *Handbook of Metalloproteins*; Messerschmidt, A., Poulos, T., Wieghardt, K., Eds.; John Wiley & Sons: Chichester, 2001.

(2) *Comprehensive Biological Catalysts*; Sinnott, M., Eds.; Academic Press: San Diego, 1998.

(3) *Biochemie*; Voeth, D., Voet, J. G., Eds.; VCH: Weinheim, 1992.

(4) *Biochemistry of Signal Transduction and Regulation*; Krauss, G., Ed.; Wiley-VCH: Weinheim, 1999.

(5) Murakami, Y.; Kikuchi, J.; Hiseada, Y.; Hayashida, O. *Chem. Rev.* **1996**, *96*, 721.

(6) (a) *Inorganic Biochemistry*; Cowan, J. A., Ed.; Wiley-VCH: Weinheim, 1997. (b) *The Biological Chemistry of the Elements − The Inorganic Chemistry of Life*; Frausto da Silva, J. J. R., Williams, R. J. P., Eds.; Oxford University Press: Oxford, 2001. (c) *Bioanorganische Chemie*; Kaim, W., Schwederski, B., Eds.; Teubner Verlag: Stuttgart, 2004.

(7) Kersting, B. *Z. Anorg. Allg. Chem.* **2004**, *630*, 765.

(8) (a) Rondelez, Y.; Rager, M. N.; Duprat, A.; Reinaud, O. *J. Am. Chem. Soc.* **2002**, *124*, 1334. (b) Rondelez, Y.; Bertho, G.; Reinaud, O. *Angew. Chem.* **2002**, *114*, 1086; *Angew. Chem., Int. Ed.* **2002**, *41*, 1044. (c) Seneque, O.; Rager, M. N.; Giorgi, M.; Reinaud, O. *J. Am. Chem. Soc.* **2001**, *123*, 8442. (d) Seneque, O.; Rager, M. N.; Giorgi, M.; Reinaud, O. *J. Am. Chem. Soc.* **2000**, *122*, 6183.

(9) Hecht, S.; Fréchet, J. M. J. *Angew. Chem.* **2001**, *113*, 76.

(10) Scott, R. W. J.; Wilson, O. M.; Crooks, R. M. *J. Phys. Chem. B* **2005**, *109*, 692.

(11) Steyer, S.; Jeunesse, C.; Armspach, D.; Matt, D.; Harrowfield, J. In *Calixarenes*; Asfari, Z., Bohmer, V., Harrowfield, J. M., Vicens, J., Saadioui, M., Eds.; Kluwer Academic: Dordrecht, 2001; p 513.

(12) Cram, D. J.; Tanner, M. E.; Thomas, R. *Angew. Chem.* **1991**, *103*, 1048; *Angew. Chem., Int. Ed. Engl.* **1991**, *30*, 1024.

(13) Chapman, R. G.; Sherman, J. C. *Tetrahedron* **1997**, *53*, 15911.

(14) Hof, F.; Craig, S. L.; Nuckolls, C.; Rebek, J. *Angew. Chem.* **2002**, *114*, 1556; *Angew. Chem., Int. Ed.* **2002**, *41*, 1488.

(15) (a) Jasat, A.; Sherman, J. C. *Chem. Rev.* **1999**, *99*, 931. (b) Barrett, E. S.; Irwin, J. L.; Edwards, A. J.; Sherburn, M. S. *J. Am. Chem. Soc.* **2004**, *126*, 16747.

(16) (a) Warmuth, R.; Yoon, J. *Acc. Chem. Res.* **2001**, *34*, 95. (b) Marquez, C.; Nau, W. M. *Angew. Chem.* **2001**, *113*, 4515; *Angew. Chem., Int. Ed.* **2001**, *40*, 4387. (c) Breslow, R. *Acc. Chem. Res.* **1995**, *28*, 146. (d) Goto, K.; Okazaki, R. *Liebigs Ann.* **1997**, 2393. (e) Ihm, C.; Kim, M.; Ihm, H.; Paek, K. *J. Chem. Soc., Perkin Trans. 2* **1999**, 1569. (f) Mendoza, S.; Davidov, P. D.; Kaifer, A. E. *Chem.—Eur. J.* **1998**, *4*, 864. (g) Warmuth, R.; Makowiec, S. *J. Am. Chem. Soc.* **2005**, *127*, 1084.

(17) Vriezema, D. M.; Aragonès, M. C.; Elemans, J. A. A. W.; Cornelissen, J. J. L. M.; Rowan, A. E.; Nolte, R. J. M. *Chem. Rev.* **2005**, *105*, 1445.

(18) Xu, W.; Vittal, J. J.; Puddephat, R. J. *Inorg. Chem.* **1997**, *36*, 86.

(19) (a) Jacopozzi, P.; Dalcanale, E. *Angew. Chem.* **1997**, *109*, 665; *Angew. Chem., Int. Ed. Engl.* **1997**, *36*, 613. (b) Fochi, F.; Jacopozzi, P.; Wegelius, E.; Rissanen, K.; Cozzini, P.; Marastoni, E.; Fisicaro, E.; Manini, P.; Fokkens, R.; Dalcanale, E. *J. Am. Chem. Soc.* **2001**, *123*, 7539.

(20) (a) Fox, O. D.; Dalley, N. K.; Harrison, R. G. *J. Am. Chem. Soc.* **1998**, *120*, 7111. (b) Fox, O. D.; Leung, J. F. Y.; Hunter, J. M.; Dalley, N. K.; Harrison, R. G. *Inorg. Chem.* **2000**, *39*, 783. (c) Harrison, R. G.; Fox, O. D.; Meng, M. O.; Dalley, N. K.; Barbour, L. J. *Inorg. Chem.* **2002**, *41*, 838.

(21) Fox, O. D.; Drew, M. G. B.; Beer, P. D. *Angew. Chem.* **2000**, *112*, 139; *Angew. Chem., Int. Ed. Engl.* **2000**, *39*, 135.

(22) (a) Lücking, U.; Chen, J.; Rudkevich, D. M.; Rebek, J. *J. Am. Chem. Soc.* **2001**, *123*, 9929. (b) Kobayashi, K.; Yamada, Y.; Yamanaka, M.; Sei, Y.; Yamaguchi, K. *J. Am. Chem. Soc.* **2004**, *126*, 13896. (c) Amrhein, P.; Shivanyuk, A.; Johnson, D. W.; Rebek, J. *J. Am. Chem. Soc.* **2002**, *124*, 10349. (d) Pinalli, R.; Cristini, V.; Sottili, V.; Geremia, S.; Campagnolo, M.; Caneschi, A.; Dalcanale, E. *J. Am. Chem. Soc.* **2004**, *126*, 6516.

(23) Flauaus, M.; Herzing, M.; Köllhofer, A.; Laly, M.; Plenio, H. *Eur. J. Org. Chem.* **2001**, 1061.

(24) Carcerands and hemicarcerands are molecules with internal voids. Guest molecules trapped inside a carcerand cannot escape from the inside on an observable time scale unless covalent bonds are broken. In hemicarcerands, exchange reactions are possible without breaking covalent bonds.

(25) Chapman, R. G.; Sherman, J. C. *J. Org. Chem.* **1998**, *63*, 4103.

(26) Cram, D. J.; Tunstad, L. M.; Knobler, C. B. *J. Org. Chem.* **1992**, *57*, 528.

(27) Cram, D. J.; Tanner, M. E.; Knobler, C. B. *J. Am. Chem. Soc.* **1991**, *113*, 7717. This open hemicarcerand is rather special since the bridging unit between the two cavitand shells is very long (quinoxaline). Obviously, with such bridging units the two cavitand shells act independently of each other (with respect to the orientation), and we cannot expect any preference for an open or closed structure.

(28) Gemperle, C.; Aebli, G.; Schweiger, A.; Ernst, R. R. *J. Magn. Reson.* **1990**, *88*, 241.

(29) Hay, P. J.; Wadt, W. R. *J. Chem. Phys.* **1985**, *82*, 299. The LACV3P basis set is a triple-ζ contraction of the LACVP basis set developed and tested at Schrödinger, Inc.

(30) *Jaguar*, version 6.0; Schrödinger, LLC, New York, 2005.

(31) Immel, S. *MolArch*$^+$ *− MOLecular ARCHitecture Modeling Program*, version 7.70; Technical University of Darmstadt, Germany, 2005.

(32) (a) Connolly, M. L. *J. Appl. Crystallogr.* **1983**, *16*, 548. (b) Connolly, M. L. *Science* **1983**, *221*, 709.

(33) Peisach, J.; Blumberg, W. E. *Arch. Biochem. Biophys.* **1974**, *165*, 691.

(34) Branca, M.; Dessi, A.; Micera, G.; Sanna, D. *Inorg. Chem.* **1993**, *32*, 578.

(35) Mims, W. B.; Peisach, J. *J. Chem. Phys.* **1978**, *69*, 4921.